Robust Predictive Current Control of PMLSM With Extended State Modeling Based Kalman Filter: For Time-Varying Disturbance Rejection

Rui Yang, Mingyi Wang, Liyi Li, *Senior Member, IEEE*, Gaolin Wang, *Senior Member, IEEE*, and Chengbao Zhong

***Abstract*—This paper proposed a robust deadbeat predictive current control (PCC) of the permanent magnet linear synchronous machine (PMLSM) with an extended state modeling (ESM) based Kalman filter (KF) for both the state and disturbance estimation. First, the disturbance dynamics of the PMLSM electrical subsystem is analyzed in detail and then the ESM is constructed as considering the disturbance as a higher order integrator motivated by the main idea of the extended state observer. Second, the KF for the current prediction with reduced noises and the disturbance estimation due to the parameter variation is designed combining with the ESM. Furtherly, the robust PCC is introduced with the ESM-based KF. Finally, the parameter tuning for the ESM-based KF is discussed with the discrete simulation and then the experimental results are given under the single current closed loop and the double cascade position-current loop with linear-varying parameter. Both the simulation and experimental results verify the effectiveness of the proposed scheme.**

***Index Terms*—Disturbance, extended state, Kalman filter (KF), permanent magnet linear synchronous machine (PMLSM), predictive current control (PCC), robust.**

I. Introduction

IN RECENT years, the motion control system driven with the permanent magnet linear synchronous machine (PMLSM) has been largely promoted in the industrial applications, such as the semiconductor manufacture and inspection equipment [1], [2] and the machine tools [3], due to its prominent high-dynamic characteristics contributed with its direct-drive structure, its realizable high-performance motion with high velocity and high precision [1]–[3].

The performance of the inner current closed loop decides directly the characteristic bound of the outer loop [4]. Thus, driven by the higher and higher demand on the high-performance motion system without increasing the hardware cost largely, how to expand the current loop performance with accurate reference value tracking and high disturbance rejection abilities furtherly becomes one of the main concerns both in the industrial and academic areas [5], [6].

The predictive control that was originally introduced in the process control has been paid increasing attention in the area of power converters and drives as reviewed in [7]. Among them, the finite control set model predictive control (FCS-MPC) is one of the research hotspots due to its several advantages, such as its simpler and intuitive discretized implementation, no requirement of a modulator, and better transient response [7]. However, its high computational burden for the cost function and lower equivalent switching frequency requires higher performance microcontroller and higher sampling frequency. For both improving the steady-state performance, many improved schemes such as the multiple-vector method [8] and the long prediction horizon method [7] have been proposed. And the steady-state performance and tracking error reduction for the FCS-MPC are still required to be studied further [7].

Relatively speaking, although the space-vector modulation is needed, the deadbeat predictive current control (PCC) for the motor drive can also be easily implemented with satisfactory performance [9]. In the meanwhile, the current controller based on the traditional PI control in many industrial applications can be directly replaced without changing the microprocessor's configuration. However, the PCC is also a model-based method in essence, thus the significant drawback lies on its robustness against the parameter variation [4], [9], [10] and this is also the main focus in the practical applications and among the academic research.

As introduced in [9] and [10], the PCC can be equivalent to a proportional (P) control with high gain and some extra decoupling terms based on the measured states, i.e., the motor currents, the rotor velocity, and the known (nominal) motor parameters. The essence of its high-gain control under the PCC guarantees its high-dynamic current response, though lack of integral terms

Manuscript received February 28, 2019; revised April 27, 2019; accepted June 13, 2019. Date of publication June 18, 2019; date of current version November 12, 2019. This work was supported in part by the State Key Program of National Natural Science of China under Grant 51537002, in part by the National Natural Science of China Youth Fund under Grant 51707046, in part by the State Major Program of National Natural Science of China under Grant 51690182, and in part by the Research Fund for the National Science Foundation of China under Grant 51877054. Recommended for publication by Associate Editor L. Dalessandro. *(Corresponding author: Liyi Li.)*

R. Yang, M. Wang, L. Li, and G. Wang are with the School of Electrical Engineering and Automation, Harbin Institute of Technology, Harbin 150001, China (e-mail: hit_yangrui@163.com; hit_mywang@163.com; liliyi.hit@gmail.com; WGL818@hit.edu.cn).

C. Zhong is with the Air Conditioning Equipment and System Operation Key Laboratory of Energy Conservation, GREE Electric Appliances, Inc., Zhuhai 519000, China (e-mail: zcbsme@126.com).

Color versions of one or more of the figures in this paper are available online at http://ieeexplore.ieee.org.

Digital Object Identifier 10.1109/TPEL.2019.2923631

and (or) the incomplete model-based decoupling reduces its robustness against the endogenous parameter variation and the exogenous disturbance. Therefore, in [11] and [12], the extra integral terms with respect to the current tracking errors are added directly to the PCC for eliminating the static error caused by the parameter mismatch against the practical one. In the meanwhile, the disturbance compensation technique based on the state estimators/observers can also play a role as an integrator. Therefore, various observer designs have been applied to the PCC for the robustness improvement, such as the time delay estimation (TDE) technique [10], the Luenberger observer [13] and the adaptive disturbance observer based on the internal model principle [14], the sliding mode observers (SMOs) based on the adaptive reaching law [15], and the higher-order methods [16], [17]. With the above methods, though the static current error can be eliminated and the current dynamic response can be improved, the basic prerequisite is that the equivalent disturbance due to the parameter variation is constant or slowly varying [18], and more or less, the parameter tuning for some of the nonlinear methods such as the higher order SMOs is not explicit.

The Kalman filter (KF) is a model-based optimal state estimator for the linear system with Gaussian error statistics [19], [20], which has received large interests in industrial control systems as reviewed in [21], especially for the state estimations of the PMSM drive systems such as in [22]–[29]. The extended Kalman filter (EKF) is designed for the current predictions in [30] and [31] and then the TDE is integrated to estimate/compensate the disturbance for the PCC in [31]. Compared with the TDE where the sampled currents are directly used, the EKF-based TDE in [31] can reduce the estimation noises without the low pass filter (LPF) and further improve the current tracking performance. However, the basic assumption that the disturbance is slowly varying is also required and the high complexity of the algorithm implementation of high-dimension EKF restricts its practical application and the parameter tuning is also relatively complicated. The extended state observer (ESO) is a main component of the active disturbance rejection control [32], which models the lumped disturbance as an extended state and then both the system states and disturbance can be estimated in the same way. The same idea has been extended to construct the generalized proportional integral observer (GPIO) in [33] and then it is designed in [18] to estimate the load disturbance and the time-varying parameter uncertainties for the FCS-MPC. Similarly, in [34], a robust current controller with a P control and the PIO/IO designed for the remaining disturbance compensation is also presented.

Motivated by the basic theory of the KF and the main idea of the ESO or the GPIO, an extended state modeling (ESM) based KF is proposed in this paper for the robustness improvement of the PCC when facing with time-varying and nonlinear disturbance. The three main components of the PCC scheme are as follows:

1) the ESM including constructing the lumped disturbance as a higher order polynomial and then modeling the disturbance dynamics as an integrator subsystem;
2) the KF design based on the ESM for both the current and disturbance estimation;
3) the PCC design with considering the current prediction and disturbance estimation in the ESM-based KF.

The main differences compared with the method in [30] and [31] lie on that: the basic assumption for the disturbance estimation (i.e., the disturbance is slowly varying) is not required for the proposed ESM, the disturbance can be directly estimated with the ESM-based KF and the complexity of algorithm implementation reduces largely with no need to calculate the Jacobian matrix in the EKF.

The main contributions of this paper are that the state/disturbance estimation method that combines the basic theory of the ESO with the KF design is proposed in the first time with the knowledge of the author, and then its application for the robustness improvement of the PCC, the following parameter tuning method with the simulation, and the final experimental verification under linear-varying parameter are also given in detail. Accordingly, the disturbance dynamics with the characteristics of strong nonlinearity and time varying is also analyzed.

The residual parts of this paper are organized as follows. In Section II, the electrical dynamics modeling of the PMLSM and the basic problem statement for the inner current loop control are presented. Then, the ESM-KF-based PCC is proposed in Section III. Section IV gives the parameter tuning procedure for the ESM-KF and the performance verification for the ESM-KF-based PCC with the simulation results. In Section V, the experimental setup and the corresponding results are listed. Finally, conclusions are summarized in Section VI.

II. PMLSM Modeling and Problem Statement

A. Electrical Dynamics Modeling of the PMLSM

The electrical subsystem dynamics of the PMLSM under nominal parameters in terms of continuous time domain is described as [4]

$$\left.\begin{aligned}\frac{d}{dt}i_d &= \frac{1}{L_{so}}\left(u_d - R_{so}i_d + \frac{\pi}{\tau}vL_{so}i_q - f_d\right)\\ \frac{d}{dt}i_q &= \frac{1}{L_{so}}\left(u_q - R_{so}i_q - \frac{\pi}{\tau}vL_{so}i_d - \frac{\pi}{\tau}v\psi_{fo} - f_q\right)\end{aligned}\right\} \tag{1}$$

where u_q/u_d and i_q/i_d are the *d*-/*q*-axes stator voltages and currents, respectively. R_s and L_s are the stator resistance and inductance, respectively. ψ_f denotes the permanent-magnet flux linkage and v is the mover velocity. τ is the permanent magnet pole pitch. The subscript "o" represents nominal value and f_d, f_q represent the lumped disturbance caused by the parameter uncertainties and the un-modeled dynamics, and they can be derived as

$$\left.\begin{aligned}f_d &= \Delta R_s i_d + \Delta L_s\frac{d}{dt}i_d - \frac{\pi}{\tau}v\Delta L_s i_q + \varepsilon_d\\ f_q &= \Delta R_s i_q + \Delta L_s\frac{d}{dt}i_q + \frac{\pi}{\tau}v\Delta L_s i_d + \frac{\pi}{\tau}v\Delta\psi_f + \varepsilon_q\end{aligned}\right\} \tag{2}$$

where $R_s = R_{so} + \Delta R_s, L_s = L_{so} + \Delta L_s, \psi_f = \psi_{fo} + \Delta\psi_f$, $\varepsilon_d, \varepsilon_q$ are the lumped un-modeled dynamics of d- and q-axes such as the voltage distortion due to the inverter deadtime, respectively.

Therefore, according to (1) and (2), the electrical dynamics can be seen as a perturbed, nonlinear, and cross-coupled system. Thus, the current control performance can be deteriorated largely especially for the model-based controller such as the PCC and the pole-placement-based PI controller.

B. Problem Statement

As can be seen from (2), the equivalent total disturbance is coupled with both the parameter variation and the system states.

The first-order time derivatives of (2) with considering the parameter variation, the current/velocity dynamics and neglecting the un-modeled dynamics as well, i.e., assuming that $\varepsilon_d, \varepsilon_q \approx 0$, can be derived and rearranged as follows:

$$\left.\begin{aligned}
&\frac{d}{dt}f_d \\
&\quad \underbrace{i_d\frac{d}{dt}\Delta R_s + \frac{d}{dt}\Delta L_s\frac{d}{dt}i_d - \omega_e i_q\frac{d}{dt}\Delta L_s} \\
&= \underbrace{+\Delta R_s\frac{d}{dt}i_d + \Delta L_s\frac{d^2}{dt^2}i_d - \omega_e\Delta L_s\frac{d}{dt}i_q} \\
&\quad \underbrace{-\Delta L_s i_q\frac{d}{dt}\omega_e} \\
&\frac{d}{dt}f_q \\
&\quad \underbrace{i_q\frac{d}{dt}\Delta R_s + \frac{d}{dt}\Delta L_s\frac{d}{dt}i_q + \omega_e i_d\frac{d}{dt}\Delta L_s + \omega_e\frac{d}{dt}\Delta\psi_f} \\
&= \underbrace{+\Delta R_s\frac{d}{dt}i_q + \Delta L_s\frac{d^2}{dt^2}i_q + \omega_e\Delta L_s\frac{d}{dt}i_d} \\
&\quad \underbrace{+\Delta L_s i_d\frac{d}{dt}\omega_e + \Delta\psi_f\frac{d}{dt}\omega_e}
\end{aligned}\right\} \tag{3}$$

where $\omega_e = \frac{\pi}{\tau}v$. Equation (3) shows the complicated time-varying characteristics of the disturbance dynamics and they can be categorized into three aspects: the effects of parameter variation with time, the current, and velocity dynamics.

For intuitive demonstration, the following preliminary and practical assumptions between the two consecutive current control instants are made:

A1) the d- and q-axes current control is decoupled sufficiently and $i_d^* = 0$ is applied, i.e., $i_d, d/dt\,(i_d)$, $d^2/dt^2\,(i_d) \approx 0$ are maintained well;

A2) the parameter mismatch is time invariant or slowly varying, i.e., $d/dt\,(\Delta R_s, \Delta L_s, \Delta\psi_f) \approx 0$.

Then, the disturbance dynamics of f_d, f_q can be further simplified as

$$\left.\begin{aligned}
\frac{d}{dt}f_d &= -\omega_e\Delta L_s\frac{d}{dt}i_q - \Delta L_s i_q\frac{d}{dt}\omega_e \\
\frac{d}{dt}f_q &= \Delta R_s\frac{d}{dt}i_q + \Delta L_s\frac{d^2}{dt^2}i_q + \Delta\psi_f\frac{d}{dt}\omega_e
\end{aligned}\right\} \tag{4}$$

which indicates the following two conclusions.

C1) The d-axis disturbance dynamics is remarkable especially as the PMLSM operates under position command with high velocity, high acceleration ($d/dt\,(\omega_e)$ is large), and high jerk (the time derivative of the acceleration, i.e., $d/dt\,(i_q)$ is large), whereas the load is heavy (i_q is large) and large inductance mismatch also exists (ΔL_s is large), that is to say, the d-axis current control cannot be completely decoupled with the q-axis dynamics as f_d being not well compensated and the assumption or the practical demand A1) cannot be maintained.

C2) The q-axis disturbance dynamics is non-negligible as the PMLSM operates under the position command with high acceleration, high jerk, and high snap (i.e., the time derivative of the jerk), whereas large system parameter mismatch also exists ($\Delta R_s, \Delta L_s, \Delta\psi_f$ are large), that is to say, the q-axis current transient response can be largely deteriorated as f_q being not well rejected.

As the above assumptions A1) and A2) are not satisfied, which is also general in practice, much more complicated disturbance dynamics is imaginable. Therefore, *the two basic but important problems are how to describe the disturbance dynamics effectively and then how to reject its influence with the controller design*. Thus, an ESM method and the corresponding KF design for both the state and disturbance estimations will be proposed to release the above two problems within the PCC in the following section.

III. ESM-KF-Based PCC

A. Extended State Modeling

According to (3), though the disturbance dynamics is time varying and significantly coupled with the parameter mismatch, the system states, and their dynamics, the local Taylor polynomial expansion with respect to the time t can also be utilized here as [33]

$$f_{dq} = \sum_{j=0}^{n-1} a_j t^j + \eta\,(t) \tag{5}$$

where n is the order, $a_j (j = 0, \ldots, n-1)$ are the polynomial coefficients, $\eta\,(t)$ is the residual part with smaller and bounded consecutive time derivatives, i.e., $|\eta^{(k)}(t)| \approx 0,\ k = 0, \ldots, n-1$ and $|f_{dq}^{(k)}(t)| = |\eta^{(k)}(t)| \approx 0$ as $k \geq n$. That is to say, the basic requirement for the disturbance is that the low-frequency parts can be simply modeled as a polynomial with finite order and the high-frequency components of the nonlinear disturbance can be neglected. Fortunately, according to (2), the disturbance can be expected to be time continuous and derivative limited due to that both the dc bus voltage of the inverter and the change rate

of the parameter mismatch are limited in general. However, as the ESM is expanded to other areas, the above requirement must be noticed, such as the friction modeling that is strictly nonlinear.

The disturbance dynamics of (3) can be approximated as the following nth-order integrator subsystems:

$$\left.\begin{aligned} f_{dq}^{(1)} &= \sum_{j=1}^{n-1} j a_j t^{j-1} = h_{dq}^1 \\ f_{dq}^{(2)} &= \sum_{j=2}^{n-1} j\,(j-1)\,a_j t^{j-2} = h_{dq}^2 \\ &\vdots \\ f_{dq}^{(n)} &= 0 = h_{dq}^n \end{aligned}\right\} \tag{6}$$

and then combining with (3), the entire $(2n+2)$th-order extended-state model can be obtained as

$$\left.\begin{aligned} \dot{i}_d &= \frac{1}{L_{so}}\left(u_d - R_{so} i_d + \omega_e L_{so} i_q - f_d\right) \\ \dot{i}_q &= \frac{1}{L_{so}}\left(u_q - R_{so} i_q - \omega_e L_{so} i_d - \omega_e \psi_{fo} - f_q\right) \\ f_d^{(1)} &= h_d^1,\ f_q^{(1)} = h_q^1 \\ &\vdots \\ f_d^{(n)} &= h_d^n,\ f_q^{(n)} = h_q^n \end{aligned}\right\} \tag{7}$$

where $h_{dq}^j, j = 1, \ldots, n$, denotes the jth time derivatives of f_{dq}.

As the zero-order hold method is used, (7) can be discretized and rearranged as

$$\left.\begin{aligned} i_d(k+1) &= \left(1 - T_s\frac{R_{so}}{L_{so}}\right) i_d(k) + \omega_e(k)\, T_s i_q(k) \\ &\quad - \frac{T_s}{L_{so}} f_d(k) + \frac{T_s}{L_{so}} u_d(k) \\ i_q(k+1) &= -\omega_e(k)\, T_s i_d(k) + \left(1 - T_s\frac{R_{so}}{L_{so}}\right) i_q(k) \\ &\quad - \frac{T_s}{L_{so}} f_q(k) + \frac{T_s}{L_{so}}\left(u_q(k) - \omega_e(k)\,\psi_{fo}\right) \\ f_d(k+1) &= f_d(k) + f_d^{(1)}(k)\, T_s \\ f_q(k+1) &= f_q(k) + f_q^{(1)}(k)\, T_s \\ &\vdots \\ f_d^{(n-1)}(k+1) &= f_d^{(n-1)}(k) \\ f_q^{(n-1)}(k+1) &= f_q^{(n-1)}(k) \end{aligned}\right\} \tag{8}$$

where T_s is the sampling period and k is the discrete sampling instant. And then (8) can be further represented in the discrete-time extended-state space as

$$\left.\begin{aligned} \boldsymbol{x}(k+1) &= \boldsymbol{A}_d \boldsymbol{x}(k) + \boldsymbol{B}_d \boldsymbol{u}(k) + \boldsymbol{\omega}(k) \\ \boldsymbol{y}(k) &= \boldsymbol{C}_d \boldsymbol{x}(k) + \boldsymbol{v}(k) \end{aligned}\right\} \tag{9}$$

where the state vector is $\boldsymbol{x} = \left[i_d \;\; i_q \;\; f_d \;\; f_q \;\; \ldots \;\; f_d^{(n-1)} \;\; f_q^{(n-1)}\right]^T$, the control input vector is $\boldsymbol{u} = [u_d \; u_q - \omega_e \psi_{fo}]^T$, $\boldsymbol{\omega} = [\omega_1 \; \omega_2 \; \ldots \; \omega_{2n+2}]^T$ denotes the process noises with the covariance $\boldsymbol{Q} = E\left\{\boldsymbol{\omega}[k]\,\boldsymbol{\omega}[k]^T\right\} > 0$ and it is modeled as the process uncertainty, $\boldsymbol{v} = [v_d \; v_q]^T$ is the measurement noise vector with the covariance $\boldsymbol{R} = E\left\{\boldsymbol{v}[k]\,\boldsymbol{v}[k]^T\right\} \geq 0$, and the covariances $\boldsymbol{Q}$ and $\boldsymbol{R}$ are reasonably assumed to be diagonal matrices with constant terms in the following KF design [23], the cross-covariance matrix satisfies $E\left\{\boldsymbol{w}[k]\boldsymbol{v}[k]^T\right\} = 0$, the measurement output vector is $\boldsymbol{y} = [i_d \; i_q]^T$, the system matrices are

$$\boldsymbol{A}_d = \boldsymbol{I}_{(2n+2)\times(2n+2)} - T_s \begin{bmatrix} \frac{R_{so}}{L_{so}} & \omega_e(k) & \frac{-1}{L_{so}} & 0 & 0 & 0 & \cdots & 0 & 0 \\ -\omega_e(k) & \frac{R_{so}}{L_{so}} & 0 & \frac{-1}{L_{so}} & 0 & 0 & \cdots & 0 & 0 \\ 0 & 0 & 0 & 0 & 1 & 0 & \cdots & 0 & 0 \\ 0 & 0 & 0 & 0 & 0 & 1 & \cdots & 0 & 0 \\ \vdots & \vdots & \vdots & \ddots & \ddots & \ddots & \ddots & 0 & 0 \\ 0 & 0 & 0 & 0 & 0 & 0 & 0 & 1 & 0 \\ 0 & 0 & 0 & 0 & 0 & 0 & 0 & 0 & 1 \\ 0 & 0 & 0 & 0 & 0 & 0 & 0 & 0 & 0 \\ 0 & 0 & 0 & 0 & 0 & 0 & 0 & 0 & 0 \end{bmatrix}$$

$$\boldsymbol{B}_d = \frac{T_s}{L_{so}} \begin{bmatrix} 1 & 0 & 0 & 0 \\ 0 & 1 & 0 & 0 \end{bmatrix}^T$$

$$\boldsymbol{C}_d = \begin{bmatrix} 1 & 0 & 0 & \cdots & 0 \\ 0 & 1 & 0 & \cdots & 0 \end{bmatrix}.$$

Assuming that the velocity dynamics is remarkably slower than the current dynamics, which is also reasonable in general, then the matrix $\boldsymbol{A}_d$ can be seen as constant between the two consecutive current control periods with $\omega_e(k)$ calculated at time k, i.e., $\boldsymbol{A}_d(k+1) \approx \boldsymbol{A}_d(k)$. Therefore, the extended-state model (9) can be seen as a linear uncertain dynamic system and then the KF can be utilized to obtain optimal estimations for both the system states and the disturbance.

B. ESM-Based KF Design

The recursive implementation procedure of the *KF Algorithm* is listed as follows [21].

The time update step: *a priori* prediction

1) State prediction

$$\boldsymbol{x}_p(k+1) = \boldsymbol{A}_d \boldsymbol{x}_e(k) + \boldsymbol{B}_d \boldsymbol{u}(k) \tag{10}$$

where $\boldsymbol{x}_p(k+1)$ is the state prediction at time $k+1$ and $\boldsymbol{x}_e(k)$ is the previously deduced state estimation at time k.

2) Prediction error covariance matrix calculation

$$\boldsymbol{P}_p(k) = \boldsymbol{A}_d \boldsymbol{P}_e(k-1) \boldsymbol{A}_d^T + \boldsymbol{Q} \tag{11}$$

where $\boldsymbol{P}_p(k)$ is the prediction error covariance matrix at time k and $\boldsymbol{P}_e(k-1)$ is the estimation error covariance matrix at time $k-1$, $\boldsymbol{Q}$ is the covariance matrix of the process noises.

3) Kalman gain calculation

$$\boldsymbol{K}(k) = \boldsymbol{P}_p(k) \boldsymbol{C}_d^T \left(\boldsymbol{C}_d \boldsymbol{P}_p(k) \boldsymbol{C}_d^T + \boldsymbol{R} \right)^{-1} \tag{12}$$

where $\boldsymbol{R}$ is the covariance matrix of the measurement noises.

The measurement update step: *A posteriori* correction

4) Estimation update with measurement

$$\boldsymbol{x}_e(k+1) = \boldsymbol{x}_p(k+1) + \boldsymbol{K}(k) \left(\boldsymbol{y}(k) - \boldsymbol{C}_d \boldsymbol{x}_p(k) \right). \tag{13}$$

5) Estimation error covariance matrix update

$$\boldsymbol{P}_e(k) = \left(\boldsymbol{I} - \boldsymbol{K}(k) \boldsymbol{C}_d \right) \boldsymbol{P}_p(k). \tag{14}$$

6) Return to (1).

Compared with the EKF-based current estimation method in [30] and [31], there exist two outstanding conveniences: 1) the online calculation burden of the state transition matrix $\boldsymbol{A_d}$ is released largely, and 2) both the currents and disturbance of the d- and q-axes can be optimally estimated simultaneously, whereas the TDE (which is proposed in [10] and utilized in [30]) and the corresponding LPF can be omitted here.

It is noted that the KF can be simply designed with (10)–(14), and the decisive point in the design is the tuning of the covariance matrices $\boldsymbol{P}_e(0)$, $\boldsymbol{Q}$, $\boldsymbol{R}$ and the selection of the initial state estimate $\boldsymbol{x}_e(0)$, which directly affect the dynamic performance and convergence speed of the KF. As pointed out in [23], the initialization value of $\boldsymbol{P}_e(0)$ mainly affects the transient amplitude of the state estimation, whereas the transient time and steady-state process will remain uninfluenced. Thus, it is more relaxed for the selection of $\boldsymbol{P}_e(0)$. The matrix $\boldsymbol{Q}$ represents the level of process noises and model uncertainty. Increasing the elements of the matrix $\boldsymbol{Q}$ will enlarge the KF gain and thus leading to faster filter dynamic. However, over-designing the elements of the matrix $\boldsymbol{Q}$ will also enhance the effect of measurement update and thus amplify the side effect of measurement noises. The matrix $\boldsymbol{R}$ indicates the characteristics of the measurement noises. Large values in the matrix $\boldsymbol{R}$ mean low confidence of the measurement, and then the filter dynamic performance will be reduced. In practice, the matrix $\boldsymbol{R}$ can be tuned preliminarily with the tested results, such as calculating with the sampled currents directly. Intuitively, the ratio of the corresponding elements in the matrices $\boldsymbol{Q}$ and $\boldsymbol{R}$ decides the KF bandwidth [21], [23]. For the measurable and unmeasurable system states, the initial estimation $\boldsymbol{x}_e(0)$ can be simply designed as the measured results [e.g., for $i_{d,e}(0)$ and $i_{q,e}(0)$] and zeros [e.g., for $f_{d,e}(0)$ and $f_{q,e}(0)$], respectively. Among these four main parameters, the elements of the covariance matrix $\boldsymbol{Q}$ play a decisive role relatively in optimizing the filter transient and steady-state performance [26]. Thus, the detailed parameter tuning for the matrix $\boldsymbol{Q}$ will be discussed in the following section with simulation.

C. ESM-KF-Based PCC Design

The traditional deadbeat PCC without the disturbance compensation but with considering the one-step delay problem in the digital control can be designed with the following two steps [4], [9]–[18].

Step 1: The d- and q-axes current predictions for the next control instant $k+1$ with

$$\left.\begin{aligned} \hat{i}_d(k+1) = {} & \left(1 - T_s \frac{R_{so}}{L_{so}}\right) i_d(k) \\ & + \omega_e(k) T_s i_q(k) \\ & + \frac{T_s}{L_{so}} u_d(k) \\ \hat{i}_q(k+1) = {} & -\omega_e(k) T_s i_d(k) \\ & + \left(1 - T_s \frac{R_{so}}{L_{so}}\right) i_q(k) \\ & + \frac{T_s}{L_{so}} \left(u_q(k) - \omega_e(k) \psi_{fo}\right) \end{aligned}\right\}. \tag{15}$$

Step 2: The d- and q-axes voltage command calculations for the next control instant $k+1$ with

$$\left.\begin{aligned} u_{d,\text{ref}}(k+1) = {} & L_{so} \frac{i_{d,\text{ref}}(k+2) - \hat{i}_d(k+1)}{T_s} \\ & + R_{so} \hat{i}_d(k+1) \\ & - \frac{\pi}{\tau} \hat{v}(k+1) L_{so} \hat{i}_q(k+1) \\ u_{q,\text{ref}}(k+1) = {} & L_{so} \frac{i_{q,\text{ref}}(k+2) - \hat{i}_q(k+1)}{T_s} \\ & + R_{so} \hat{i}_q(k+1) \\ & + \frac{\pi}{\tau} \hat{v}(k+1) L_{so} \hat{i}_d(k+1) \\ & + \frac{\pi}{\tau} \hat{v}(k+1) \psi_{fo} \end{aligned}\right\} \tag{16}$$

where $\hat{v}(k+1)$ is the estimated mover velocity of the next instant $k+1$, which is assumed as $\hat{v}(k+1) \doteq v(k)$ due to the velocity dynamics is generally much slower than the current response and can be simply calculated with the backward differentiation method as the high-resolution linear encoder is utilized, and $i_{dq,\text{ref}}(k+2)$ is defined as $i_{dq,\text{ref}}(k+2) \doteq i_{dq}^*(k)$ in

which $i^*_{dq}(k)$ is the output of the outer loop position or velocity controller.

Remark 1: As shown in (16), the PCC can be simply interpreted as a high-gain P control, whereas the integral term in the traditional PI control has been replaced with the additional model-based feedforward compensation terms. The gain L_{so}/T_s is proportional to the inductance parameter in the PCC and inversely proportional to the current control period (equal to the switching period in this paper under the single-sampling-single-update strategy). Thus, to some extent, the selection of the current control period depends on the motor inductance and the noise amplitude of the current sampling.

As the proper order for the disturbance f_d, f_q approximation is selected, the KF Algorithm can be applied to the ESM of (9), and then the estimations of $\boldsymbol{i}_{dq,e}(k+1)$, $\boldsymbol{f}_{dq,e}(k+1)$ can be directly obtained for the next control instant $k+1$.

Compared with the estimation method in (15), both the parameter uncertainty and the current sampling noise effect can be considered in the *KF Algorithm*. Thus, referring to (16), the voltage commands with the ESM-based KF are revised as

$$\left.\begin{aligned} u_{d,\mathrm{ref}}(k+1) = {} & L_{so}\frac{i_{d,\mathrm{ref}}(k+2)-i_{d,e}(k+1)}{T_s} \\ & + R_{so}i_{d,e}(k+1) \\ & - \frac{\pi}{\tau}\hat{v}(k+1)L_{so}i_{q,e}(k+1) \\ & + f_{d,e}(k+1) \\ u_{q,\mathrm{ref}}(k+1) = {} & L_{so}\frac{i_{q,\mathrm{ref}}(k+2)-i_{q,e}(k+1)}{T_s} \\ & + R_{so}i_{q,e}(k+1) \\ & + \frac{\pi}{\tau}\hat{v}(k+1)L_{so}i_{d,e}(k+1) \\ & + \frac{\pi}{\tau}\hat{v}(k+1)\psi_{fo} + f_{q,e}(k+1) \end{aligned}\right\}. \quad (17)$$

Remark 2: As shown in (17), the noise-reduced estimations of $i_{d,e}(k+1)$, $i_{q,e}(k+1)$ from the ESM-based KF replace the inaccurate and noisy predictions in (15), whereas in (17), the parameter uncertainty has also been considered both for the current estimation and the voltage command calculation. Thus, lower current noises and robustness improvement can be expected in our proposed ESM-KF-based PCC with (9)–(14) and (17).

For considering the voltage source inverter (VSI) saturation limit, the following modification of the command voltage should be applied [31]:

$$\boldsymbol{u}_{\mathrm{ref}} = \begin{cases} \boldsymbol{u}_{\mathrm{ref}}(k+1) & u_{\mathrm{ref}}(k+1) \leqslant U_{\mathrm{dc}}/\sqrt{3} \\ \dfrac{U_{\mathrm{dc}}/\sqrt{3}}{u_{\mathrm{ref}}(k+1)}\boldsymbol{u}_{\mathrm{ref}}(k+1) & u_{\mathrm{ref}}(k+1) \geqslant U_{\mathrm{dc}}/\sqrt{3} \end{cases} \quad (18)$$

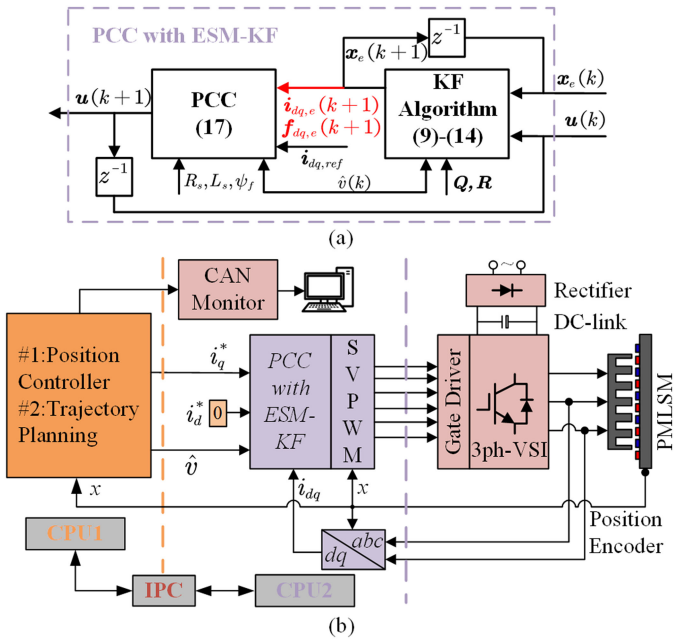

Fig. 1. (a) Block diagram of the PCC with the ESM-KF and (b) the double cascade position-current control system for the PMLSM.

TABLE I
MAIN PARAMETERS OF THE TESTED PMLSM

Parameters	Values	Unit
Nominal/Maximum thrust	600/1200	N
Thrust coefficient	94.2	N/A
Nominal velocity	0.6	m/s
Mover mass	45	kg
Stator resistance	6.5	Ω
Stator inductance	35	mH
Magnetic flux	0.24	Wb
Pole/slot number	24/18	-

with

$$u_{\mathrm{ref}}(k+1) = \|\boldsymbol{u}_{\mathrm{ref}}(k+1)\| = \sqrt{u^2_{d,\mathrm{ref}}(k+1) + u^2_{q,\mathrm{ref}}(k+1)}$$

in which U_{dc} is the dc-link voltage of the VSI. The block diagram of the PCC with the ESM-based KF is depicted in Fig. 1(a).

IV. ESM-KF PARAMETER TUNING WITH SIMULATION

For the basic *KF Algorithm* verification and the following parameter tuning, the discrete simulation model is first built in the Simulink/MATLAB. The simulation model comprises four main components: the ESM-KF-based PCC, the PMLSM drive system, the discretization sampling plus the Gaussian white noises modeled with the uniform random numbers (URNs), and the control delay existing in the real digital control system. The main parameters of the simulated PMLSM are the same as the tested platform, which will be introduced in Section V and they are listed in Table I.

As illustrated in Section III-B, the main design parameters for the KF are $\boldsymbol{x}_e(0)$, $\boldsymbol{P}_e(0)$, $\boldsymbol{Q}$, and $\boldsymbol{R}$. *First*, the initial estimates of $i_{d,e}, i_{q,e}$ can be simply initialized as the sampled currents of the d- and q-axes, respectively, which will also be used in the experimental tests as given in the following section. Assuming that the current offsets are eliminated effectively, which is also one of the main aims in the hardware design stage, then $\boldsymbol{i}_{dq,e}(0) = [0\ \ 0]^T$ can be directly set as the motor will run from the static state generally, and this will be utilized in the following simulations. Simultaneously, as shown in (2), the initial values of $f_{d,e}(0), f_{q,e}(0)$ can also be configured as zeros due to the initial currents are $\boldsymbol{i}_{dq} = 0$. Therefore, the initial values of $\boldsymbol{x}_e(0)$ can be obtained as zeros. *Second*, as the current noises are modeled as URNs, which are represented with $\boldsymbol{v}_{d,q} = \mathcal{N}\left(0, \text{diag}\left(\sigma_d^2, \sigma_q^2\right)\right)$, the covariance matrix $\boldsymbol{R}$ can be directly calculated. Thus, $\boldsymbol{R} = \text{diag}\left(\sigma_d^2, \sigma_q^2\right)$ is simply selected here as the starting point for the following fine retuning. With trial-and-error process, $\boldsymbol{R} = \text{diag}(10, 10)$ is selected. *Third*, as the initial estimation error covariance matrix $\boldsymbol{P}_e(0)$ will only affect the transient amplitude of the state estimations, it can be assumed as $\boldsymbol{0}_{(2n+2)\times(2n+2)}$ (zero matrix) temporarily. Then, the following focus will be placed on the tuning of the matrix $\boldsymbol{Q}$ to optimize the filter performance and convergence speed of the state and disturbance estimations.

A. Open-Loop Parameter Tuning

The open-loop tests are first conducted under the current closed loop with the traditional PCC, i.e., (15) and (16). The actual voltage commands and the current response are the inputs of the ESM-based KF and its output (i.e., $\boldsymbol{i}_{dq,e}, \boldsymbol{f}_{dq,e}$) are monitored for the parameter tuning. The test conditions are listed as follows:

C1) only the resistance mismatch exists ($R_s = 2R_{so}$);
C2) the current command of the q-axis is a square wave and $i_d^* = 0$ is applied;
C3) the amplitude and frequency of the current command should be selected to ensure that the mover velocity is low enough for reducing the flux mismatch effect in the real experiments.

Then, the disturbance f_q will also be expected to be a square wave, which is in phase with the i_q^*. Thus, when the Q_{11}, Q_{22} in the matrix $\boldsymbol{Q}$ have been preliminarily designed, the tuning of Q_{33}, Q_{44} can be analogous to the regulation of the P gain in the traditional PI control. In this paper, $Q_{11} = Q_{22}, Q_{33} = Q_{44}$ are simply selected and the effectiveness will both be verified with the following simulations and experiments.

As depicted in the bottom plot of Fig. 2, with Q_{33}, Q_{44} increasing, the convergence of the disturbance estimation f_q also speeds up, but the estimation noises are also amplified. Accordingly, the noises and overshoot of the q-axis current estimation $i_{q,e}$, as shown in the middle magnification plot of Fig. 2, will also be enlarged with larger values of Q_{33}, Q_{44}. As the proper range of Q_{33}, Q_{44} being settled, the Q_{11}, Q_{22} can be retuned to optimize the current estimation performance. Therefore, the selection of the elements of the matrix $\boldsymbol{Q}$ should be balanced with the noise level and convergence speed of both the state and

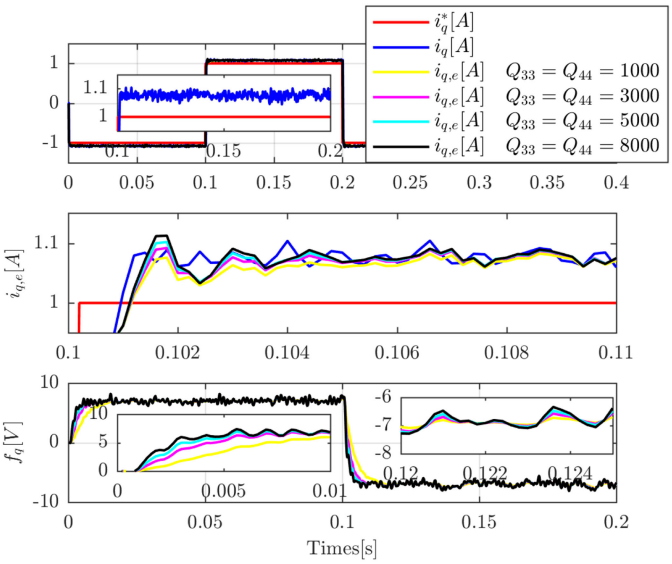

Fig. 2. Open-loop simulation results for the tuning of the matrix $\boldsymbol{Q}$ with $\boldsymbol{x}_e(0) = \boldsymbol{0}, \boldsymbol{P}_e(0) = \boldsymbol{0}, \boldsymbol{R} = \text{diag}(10, 10)$, and $\boldsymbol{Q} = \text{diag}(1, 1, Q_{33}, Q_{44})$, where $Q_{33} = Q_{44}$ and varies from 1000 to 8000.

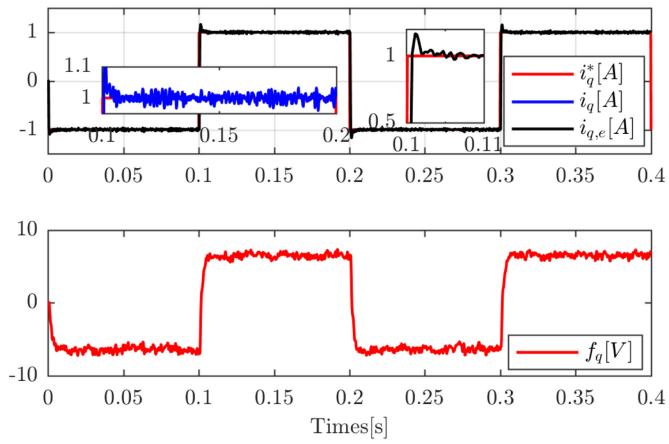

Fig. 3. Simulated current response, current estimation $i_{q,e}$, and disturbance estimation $f_{q,e}$ with the ESM-KF-based PCC in the single current closed loop under the resistance mismatch $R_s = 2R_{so}$ and $\boldsymbol{x}_e(0) = \boldsymbol{0}, \boldsymbol{P}_e(0) = \boldsymbol{0}, \boldsymbol{R} = \text{diag}(10, 10), \boldsymbol{Q} = \text{diag}(1, 1, 5000, 5000)$.

disturbance estimations with trial-and-error process. Nevertheless, with the above special designed test conditions, the tuning process can be largely simplified.

It can also be noted from (2) that, as i_d^* is a square wave and $i_q^* = 0$ is set, the above tuning process of Q_{33}, Q_{44} can also be operated but with monitoring the dynamics of $i_{d,e}$ and $f_{d,e}$. Finally, the vector $\boldsymbol{x}_e(0) = \boldsymbol{0}$ and the matrices $\boldsymbol{P}_e(0) = \boldsymbol{0}$, $\boldsymbol{R} = \text{diag}(10, 10)$, and $\boldsymbol{Q} = \text{diag}(1, 1, 5000, 5000)$ are selected in this simulation.

B. Closed-Loop Verification

Then, the closed-loop tests with the ESM-KF-based PCC (17) are conducted. As shown in Fig. 3, the static error of the current response in the top plot of Fig. 2 is eliminated with rapid and

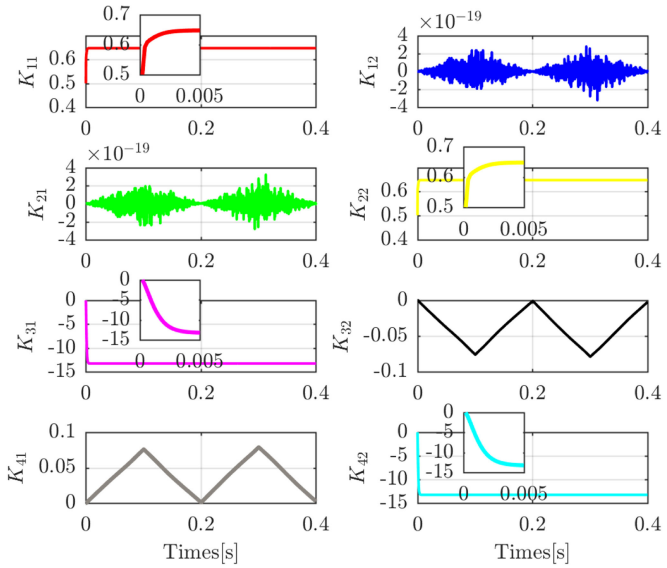

Fig. 4. Simulated Kalman gain $\boldsymbol{K}$ with the ESM-KF-based PCC in the single current closed loop under the resistance mismatch $R_s = 2R_{so}$ and $\boldsymbol{x}_e(0) = \boldsymbol{0}$, $\boldsymbol{P}_e(0) = \boldsymbol{0}$, $\boldsymbol{R} = \mathrm{diag}(10, 10)$, $\boldsymbol{Q} = \mathrm{diag}(1, 1, 5000, 5000)$.

accurate disturbance estimation, where the convergence time is about 5 ms and the amplitude of f_q is 6.5 [V] ($= R_{so} i_q^*$). The variation of the KF gains is given in Fig. 4. The following observations can be made. First, the values of $K_{11}, K_{22}, K_{31}, K_{42}$ are much larger than the remaining elements of the gain $\boldsymbol{K}$ on the order of magnitude, which is caused by the following formula expansion of (13):

$$\begin{bmatrix} i_{d,e}(k+1) \\ i_{q,e}(k+1) \\ f_{d,e}(k+1) \\ f_{q,e}(k+1) \end{bmatrix} = \begin{bmatrix} i_{d,e}(k) \\ i_{q,e}(k) \\ f_{d,e}(k) \\ f_{q,e}(k) \end{bmatrix} + \begin{bmatrix} K_{11} & K_{12} \\ K_{21} & K_{22} \\ K_{31} & K_{32} \\ K_{41} & K_{42} \end{bmatrix} \Delta \boldsymbol{i}$$

$$\Delta \boldsymbol{i} = \begin{bmatrix} i_d(k) - i_{d,p}(k+1) \\ i_q(k) - i_{q,p}(k+1) \end{bmatrix}$$

where the current and disturbance estimations of the d- and q-axes are mostly dependent on the corresponding current sampling. For example, as the cross-coupling term $-\frac{\pi}{\tau} v L_{so} i_d$, the back electromotive force $-\frac{\pi}{\tau} v \psi_{fo}$, and the disturbance $-f_q$ in (1) are effectively compensated with (17), the q-axis current dynamics can be decoupled with the d-axis. Thus, it is reasonable that the gain K_{22} is dominant in the estimation of $i_{q,e}$. Second, the gains $K_{11}, K_{22}, K_{31}, K_{42}$ converge within 5 ms, which is consistent with the state and disturbance estimation dynamics in Fig. 2. The gains K_{32}, K_{41} vary like a sawtooth, which can be contributed by the specified q-axis current command (i.e., a square wave). However, the values are smaller enough with respect to the gains K_{31}, K_{42} and then their effects can be negligible.

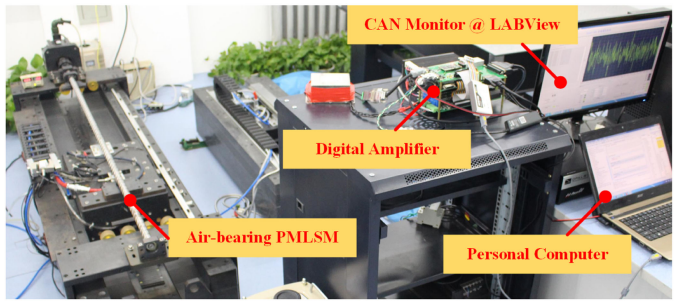

Fig. 5. Tested linear motion stage with the air-bearing iron-core PMLSM.

According to the simulation results, the effectiveness of the proposed ESM-KF-based PCC is verified. Due to the space limit, the tuning of Q_{11}, Q_{22} and the current response performance under different parameter variations (which will be given with the experimental results in the following section) are not presented here.

Remark 3: As the dimension of the state vector increases, the computational complexity of the *KF Algorithm* grows accordingly, contributing to a higher digital implementation cost. Considering that the partial elements of the KF gain are much smaller than the others, as shown in Fig. 4, the partial update scheme instead of the full update of the gains as presented in [25] can be utilized here to reduce the calculation complexity of the algorithm, with the state estimation accuracy not being much reduced. In addition, the above parameter tuning process will also be harder as the dimension of the state vector grows and the adaptive or self-tuned scheme as in [26]–[29] can be explored further.

V. Experimental Evaluation

A. Experimental Setup

To verify the effectiveness of the proposed method, as depicted in Fig. 5, a self-made air-bearing experimental stage driven with the surface-mounted iron-core PMLSM was built.

The motor was driven with a full digital power amplifier based on the 32-b floating-point TI microcontroller (MCU) TMS320F28377D with double cores. The simplified block diagram of the overall system is shown in Fig. 1(b) and the detailed hardware and software designs are listed in the following.

1) Hardware Design: The amplifier utilizes a three-phase VSI with three sets of insulated-gate bipolar transistors under the bus voltage of 310 [V], which is rectified from a single-phase ac power supply (220 VAC/50 Hz). The sampling frequency of both the position and the current loop is equal to the switching frequency (5 [kHz]) in this paper. Two-phase motor currents are measured through two LEM current sensors with accuracy of $\pm 0.2\%$. The mover position is measured through a high-resolution (0.1 μm) linear encoder. Tested results are recorded through the LabVIEW monitor with the CAN2.0 protocol, and then processed using the MATLAB.

2) Software Design: The CPU1 of the MCU is configured for outer position closed loop including the trajectory planning,

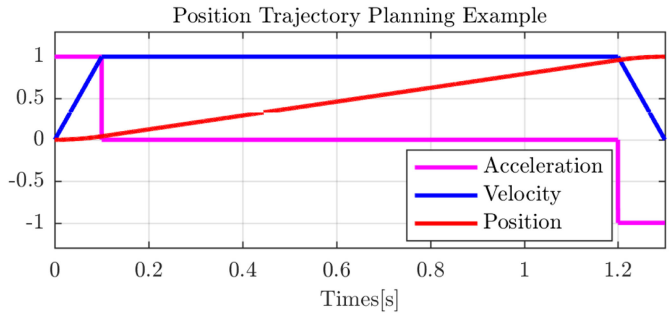

Fig. 6. Example of the normalized second-order position trajectory.

the position controller implementation, and the CAN2.0 protocol. The CPU2 is allocated for the vector control including the current sampling and processing, the coordinate transformations, the space vector pulse-width-modulation (SVPWM), and the PCC with ESM-KF, etc. The information request and share between the two CPUs is allowed through the build-in Inter-Processor Communication module.

3) Position Controller Design and Trajectory Planning: The position feedback controller is designed as the PI controller plus a lead compensator [2] with $C_{\text{fb}}(s) = K_p \dfrac{\tau s+1}{s} \dfrac{\tau_1 s+1}{\tau_2 s+1}$, where $K_p = 4.2658 \times 10^5, \tau = 0.0159, \tau_1 = 0.0265, \tau_2 = 2.653 \times 10^{-4}$. With the nominal system parameters listed in Table I, the open-loop cutoff frequency is 60 Hz and the phase margin is above 45°. The digital implementation is discretized with the Tustin method and the sampling period is $T_s = 200\ \mu$s. For evaluating the effectiveness of the proposed scheme merely, a second-order *S*-curve with limited maximum acceleration is designed in this paper and the trajectory will be implemented for the tests with double cascade position-current loop. For clear demonstration, the curves of acceleration, velocity, and position are normalized against their corresponding maximum values and an example of them is shown in Fig. 6.

B. Experimental Results

1) $\boldsymbol{x}_e(0), \boldsymbol{P}_e(0), \boldsymbol{Q}, \boldsymbol{R}$ Tuning Results: As analyzed in Section IV, the initial estimates $\boldsymbol{x}_e(0)$ are initialized as $\boldsymbol{x}_e(0) = [i_d(0)\ i_q(0)\ 0\ 0]^T$, where $i_d(0), i_q(0)$ represent the sampled currents just before the motor is running. The matrix $\boldsymbol{P}_e(0)$ is simply designed as zero matrix without reducing the steady-state estimation performance largely. The matrices $\boldsymbol{R} = \text{diag}(1,1)$ and $\boldsymbol{Q} = \text{diag}(0.2, 0.2, 200, 200)$ are finally tuned following the procedure as shown in Section IV and they will be used in all the following tests. The time consumptions of the ESM-KF-based PCC are tested with toggling the MCU pin. The calculation periods of the ESM-based KF and the PCC are 6.5 μs and 2.8 μs, respectively. Therefore, the real-time state and disturbance estimations can be done under the sampling frequency of 5 kHz in this paper or higher one.

The experimental results as only the resistance mismatch exists ($R_s = 2R_{so}$) with and without the ESM-KF are shown in Figs. 8 and 7, respectively. It can be observed that the static

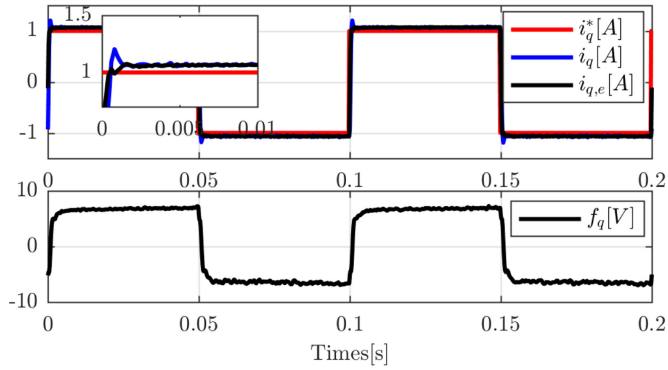

Fig. 7. Tested square-wave current response under the PCC without the ESM-KF with $\boldsymbol{x}_e(0) = [i_d(0)\ i_q(0)\ 0\ 0]^T, \boldsymbol{P}_e(0) = \boldsymbol{0}, \boldsymbol{R} = \text{diag}(1,1), \boldsymbol{Q} = \text{diag}(0.2, 0.2, 200, 200)$, as $R_s = 2R_{so}$ and $L_s = L_{so}, \psi_f = \psi_{fo}$.

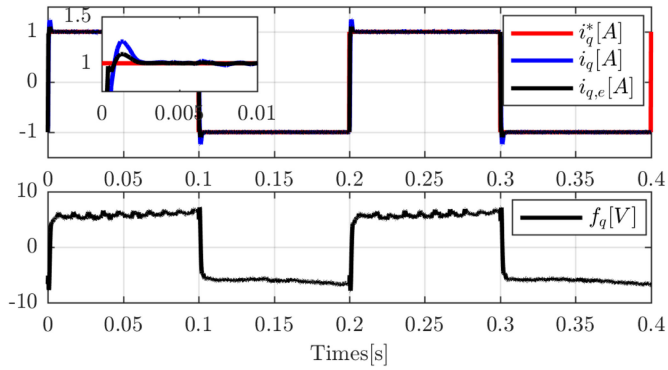

Fig. 8. Tested square-wave current response under the ESM-KF-based PCC with $\boldsymbol{x}_e(0) = [i_d(0)\ i_q(0)\ 0\ 0]^T, \boldsymbol{P}_e(0) = \boldsymbol{0}, \boldsymbol{R} = \text{diag}(1,1), \boldsymbol{Q} = \text{diag}(0.2, 0.2, 200, 200)$, as $R_s = 2R_{so}$ and $L_s = L_{so}, \psi_f = \psi_{fo}$.

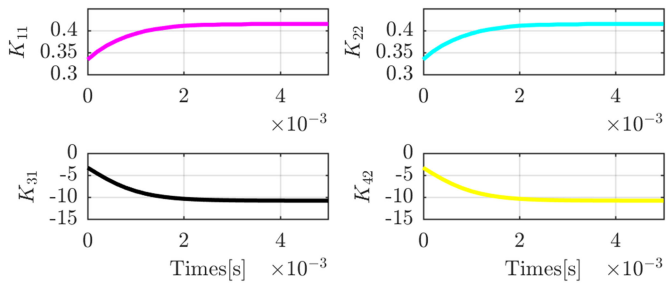

Fig. 9. Tested Kalman gains under the ESM-KF-based PCC with $\boldsymbol{x}(0) = [i_d(0)\quad i_q(0)\quad 0\quad 0]^T, \boldsymbol{P}_e(0) = \boldsymbol{0}, \boldsymbol{R} = \text{diag}(1,1), \boldsymbol{Q} = \text{diag}(0.2, 0.2, 200, 200)$, as $R_s = 2R_{so}$ and $L_s = L_{so}, \psi_f = \psi_{fo}$.

error of the q-axis current response is completely compensated and the lumped disturbance f_q and the q-axis current estimation $i_{q,e}$ are also accurately estimated. The little ripple in f_q, as shown in the bottom plot of Fig. 8 as the ESM-KF is utilized in the PCC, is caused by the current sampling noises, which can be reduced with smaller values of Q_{33}, Q_{44}. The variations of the KF gains are depicted in Fig. 9 and the convergence time is about 3–4 ms. Therefore, compared with the simulation results shown in Figs. 2–4, the experimental tests verify the validity of the proposed ESM-KF-based PCC further.

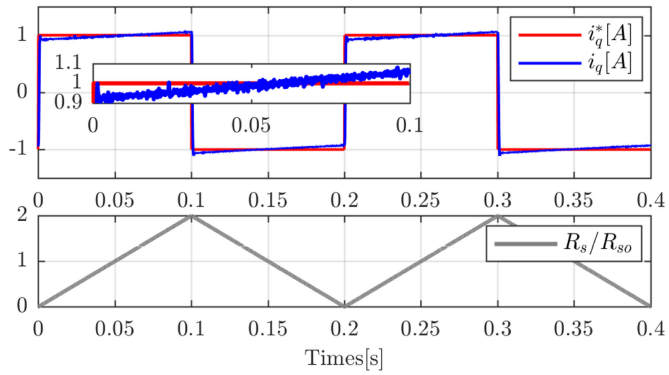

Fig. 10. Tested square-wave current response under the PCC without the ESM-KF as R_s varies within (0–2) R_{so} and $L_s = L_{so}, \psi_f = \psi_{fo}$.

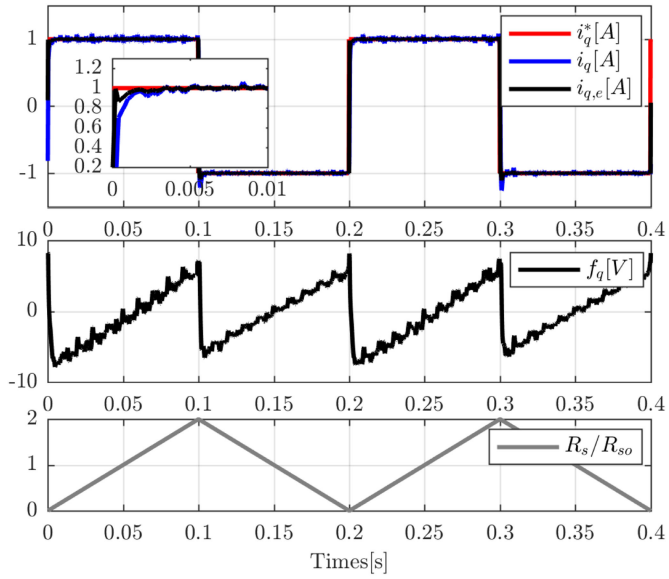

Fig. 11. Tested square-wave current response under the ESM-KF-based PCC as R_s varies within (0–2) R_{so} and $L_s = L_{so}, \psi_f = \psi_{fo}$.

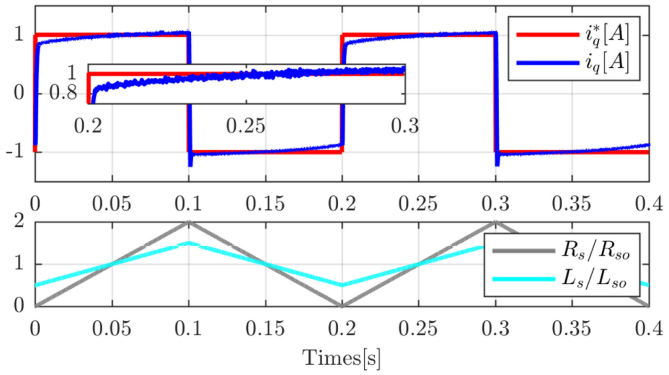

Fig. 12. Tested square-wave current response under the PCC without the ESM-KF as R_s varies within (0–2) R_{so}, L_s varies within (0.5–1.5) L_{so}, and $\psi_f = \psi_{fo}$.

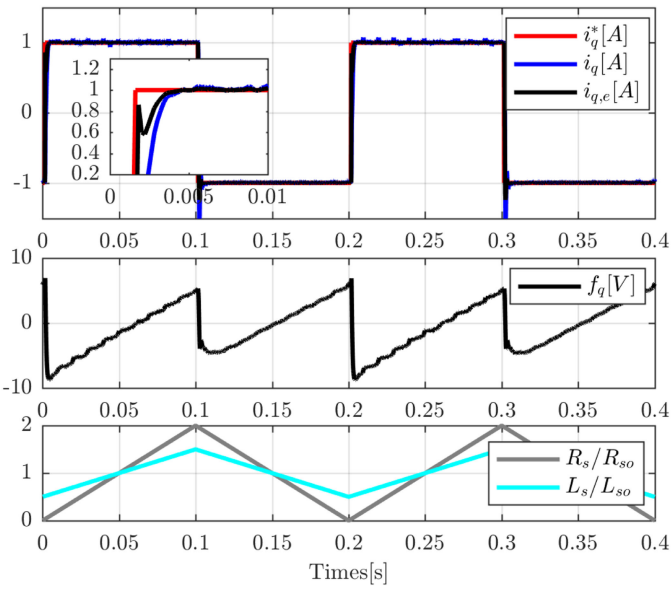

Fig. 13. Tested square-wave current response under the ESM-KF-based PCC as R_s varies within (0–2) R_{so}, L_s varies within (0.5–1.5) L_{so}, and $\psi_f = \psi_{fo}$.

2) Square-Wave Current Command Tests With Linear-Varying Parameter: To further evaluate the filter performance of the proposed ESM-KF with respect to the time-varying disturbance and the effectiveness of the proposed ESM-KF-based PCC, the conditions with the PCC parameter varying linearly in the controller are also tested.

Fig. 10 gives the q-axis current response under the PCC without the ESM-KF as the resistance varies linearly ($R_s =$ (0–2) R_{so}) with the current command. The actual q-axis current also varies linearly with the resistance profile, which is consistent with the representation in (2). As the ESM-KF-based PCC is utilized, the actual q-axis current shown in Fig. 11 tracks the command without a linear-varying static error, whereas both the lumped disturbance f_q and the q-axis current estimation $i_{q,e}$ are accurately estimated after a short transient period. The little ripple in the estimated f_q is caused by the current sampling noises and the larger values in the matrix $\boldsymbol{Q}$, which can be balanced with the estimation convergence speed through retuning the matrix $\boldsymbol{Q}$.

Figs. 12 and 13 present the current response as the inductance mismatch also exists ($L_s = (0.5\text{–}1.5)L_{so}$ under the following tests). Compared with Fig. 10, a slower current dynamic is depicted in Fig. 12 as the resistance and inductance are both underestimated at the time instant of 0 [s] and 0.2 [s]. In the contrary, a faster current response is shown as the resistance and inductance are both overestimated at the time instant of 0.1 [s] and 0.3 [s]. The difference lies on the essentially high-gain control of the PCC according to (17), where the gain L_{so}/T_s is approximately proportional to the inductance. Correspondingly, as the ESM-KF-based PCC is utilized, comparative current dynamics with Fig. 11 are also obtained in Fig. 13 while the larger overshoot at the time instant of 0.1 [s] and 0.3 [s] is caused by the larger resistance and inductance.

Furtherly, the linear-varying flux mismatch ($\psi_f = (0\text{–}2)\psi_{fo}$) is also added in the PCC. According to (2), the effect of flux mismatch is coupled with the mover velocity, and so as to clearly

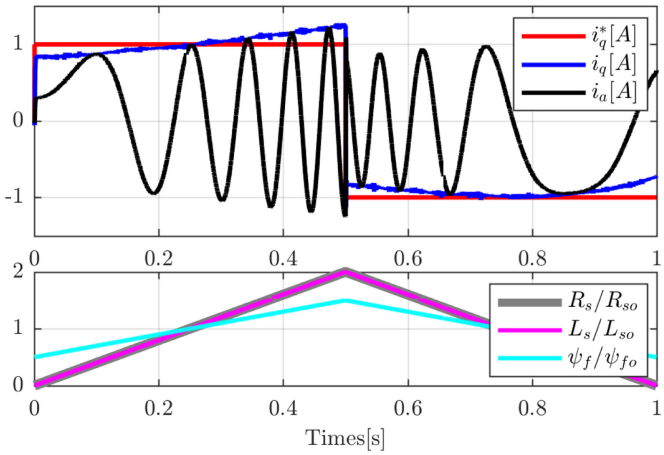

Fig. 14. Tested square-wave current response under the PCC without the ESM-KF as R_s varies within (0–2) R_{so}, L_s varies within (0.5–1.5) L_{so}, and ψ_f varies with (0–2) ψ_{fo}.

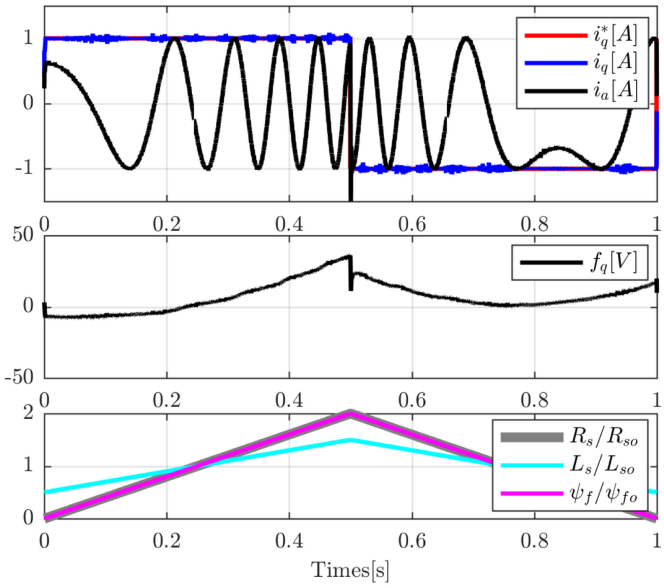

Fig. 15. Tested square-wave current response under the ESM-KF-based PCC as R_s varies within (0–2) R_{so}, L_s varies within L_{so}, and (0.5–1.5) ψ_f varies within (0–2) ψ_{fo}.

demonstrating its influence on the PCC, the frequency of the square-wave current command is adjusted to 1 [Hz] for obtaining higher velocity. As depicted in Fig. 14, the mover will be accelerated with the positive q-axis current and the current response is also increasing gradually while the peak of the phase current agrees well with the actual q-axis current. As the ESM-KF-based PCC is applied, the above current error is eliminated completely as depicted in Fig. 15. Correspondingly, the time-varying disturbance including both the effect of resistance, inductance, flux mismatch and the un-modeled dynamics, as indicated in the middle plot of Fig. 15, is well estimated online.

The tested results shown in Figs. 10–15 are further summarized in Table II. The performance comparison between the traditional deadbeat PCC without disturbance compensation and our proposed ESM-KF-based PCC is conducted qualitatively or

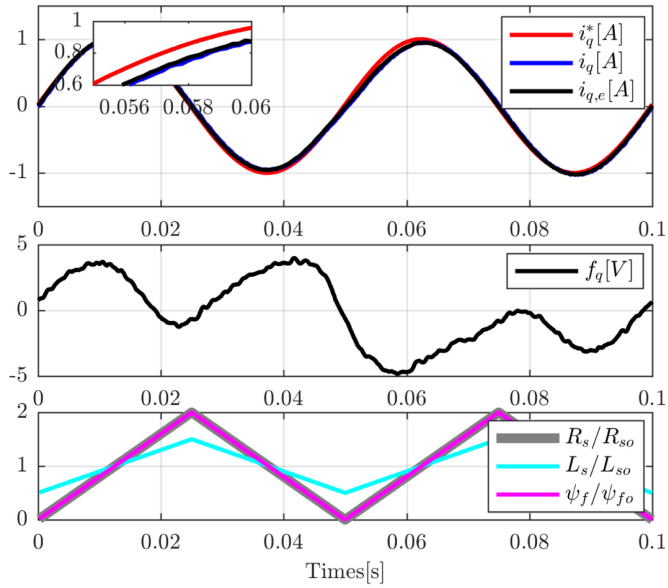

Fig. 16. Tested sine-wave current response under the PCC without the ESM-KF as R_s varies within (0–2) R_{so}, L_s varies within (0.5–l1.5) L_{so}, and ψ_f varies within (0–2) ψ_{fo}.

semiquantitatively with considering the steady-state current error and the transient current response speed as the main indexes. It can be easily noted that the PCC performance can be largely improved with our proposed ESM-based KF.

3) Sine-Wave Current Command Tests With Linear-Varying Parameter: Considering that the d- and q-axes current variations are zeros under the steady state with a square-wave current command, the terms with respect to the actual current dynamics, i.e., $d/dt\,(i_{dq})\,, d^2/dt^2\,(i_{dq})$, are much smaller. Thus, for further demonstrating the effectiveness of the ESM-KF on the estimation of the disturbance coupled with the current dynamics, the sine-wave current command tests are also conducted as follows, whereas the resistance, inductance, and flux also vary linearly with the current command under the same frequency. The magnitude and frequency of the sine-wave command are designed as 1 [A] and 20 [Hz], respectively.

As shown in Fig. 16, when the disturbance is not compensated, there exists explicit current tracking error. As the ESM-KF-based PCC is configured, the actual current tracks the command completely. The estimated disturbance f_q shown in the middle plots in Figs. 16 and 17 is seriously nonlinear and time varying, which is coincident well with the representation in (2) and (3). As the estimation of $i_{q,e}$, f_q is not used for the robustness improvement of the PCC, the estimated f_q is different with the one in the ESM-KF-based PCC, which is caused by the difference with the actual current response, as shown in the upper plots in Figs. 16 and 17.

4) Current Response Tests Under the Double Cascade Position-Current Control With Constant Parameter Mismatch: Until now, the validity of the proposed ESM-KF-based PCC has been verified in the single current closed loop. In the following, the above tests are furtherly expanded to the double cascade position-current control with constant parameter mismatch, i.e.,

TABLE II
PERFORMANCE COMPARISON BETWEEN THE TRADITIONAL AND OUR PROPOSED ESM-KF-BASED DEADBEAT PCC

Parameter mismatch	Disturbance[a]	Steady-state error		Transient response	
		traditional PCC	ESM-KF-based PCC	traditional PCC	ESM-KF-based PCC
$R_s/R_{so} \in [0,2]$	linear-varying	linear-varying	zero	slow with large error	$< 3ms$[b]
$R_s/R_{so} \in [0,2]$, $L_s/L_{so} \in [0.5,1.5]$	strictly nonlinear-varying	nonlinear-varying	zero	slow with large error	$< 4ms$[b]
$R_s/R_{so} \in [0,2]$, $L_s/L_{so} \in [0.5,1.5]$, $\psi_f/\psi_{fo} \in [0,2]$	strictly nonlinear-varying	nonlinear-varying	zero	slow with large error	$< 4ms$[b]

[a] The theoretical disturbance characteristic according to (2) as i_q^* is a square wave and $i_d^* = 0$.
[b] The rising time as i_q reaches i_q^* in the first time only when the controller parameter that is underestimated is calculated.

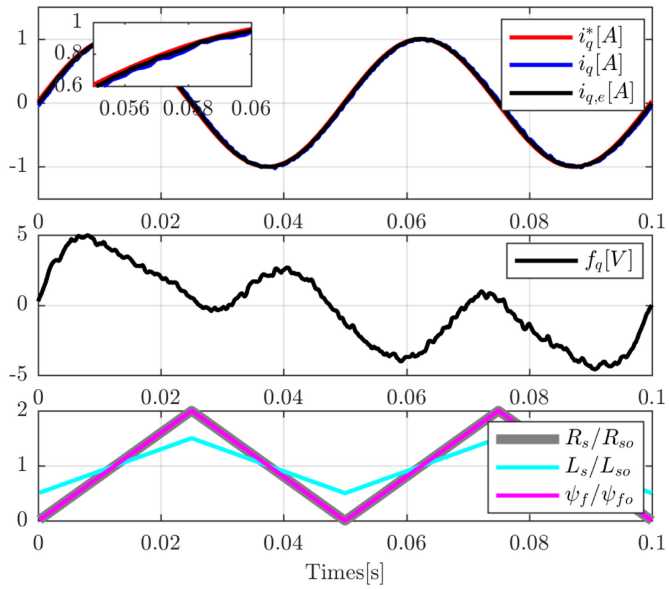

Fig. 17. Tested sine-wave current response under the ESM-KF-based PCC as R_s varies within (0–2) R_{so}, L_s varies within (0.5–1.5) L_{so}, and ψ_f varies within (0–2) ψ_{fo}.

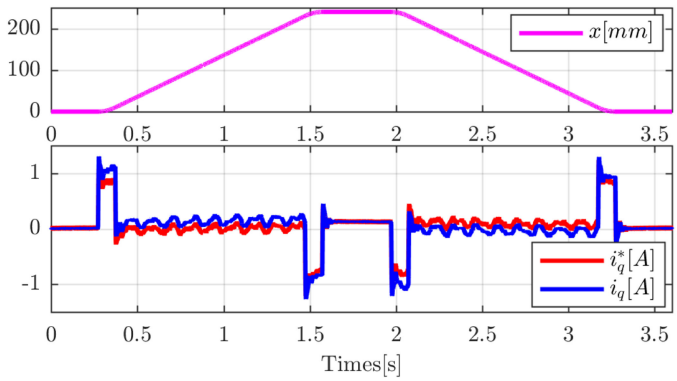

Fig. 18. Tested current response with the double cascade position-current control under PCC without the ESM-KF as $R_s = 2R_{so}, L_s = 0.5L_{so}, \psi_f = 2\psi_{fo}$.

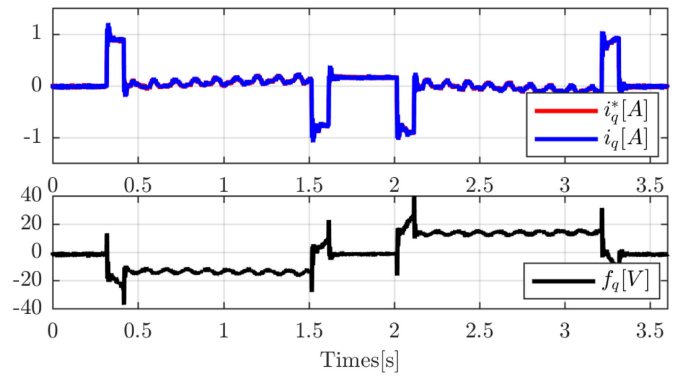

Fig. 19. Tested current response with the double cascade position-current control under the ESM-KF-based PCC as $R_s = 2R_{so}, L_s = 0.5L_{so}, \psi_f = 2\psi_{fo}$.

$R_s = 2R_{so}, L_s = 0.5L_{so}, \psi_f = 2\psi_{fo}$ (this selection is due to that it is relatively rigorous in the above mismatch conditions and then the effectiveness under other small parameter mismatch can be expected). Considering that the load cannot be added easily to the test platform, a simple second-order position trajectory command is planned with the acceleration, velocity limits are 2 m/s^2, 0.2 m/s, respectively, and the moving distance is 240 mm, where the step current command can be given from the position controller.

As indicated in Fig. 18, the current tracking error exists in the overall moving range without the ESM-KF, whereas the error is entirely eliminated in Fig. 19 under the ESM-KF-based PCC. The little current ripple in the constant velocity range is caused by the inherent force ripple of the tested stage driven with the iron-core PMLSM, and then it leads to the ripple in the estimated f_q, as depicted in the bottom plot in Fig. 19.

Therefore, the effectiveness of the proposed ESM-KF-based PCC is effectively verified under both the single current closed loop and the double closed loop with cascade position-current control. In addition, the parameter robustness limit can be guaranteed within the range of $R_s/R_{so} \in [0,2]$, $L_s/L_{so} \in [0.5,1.5]$, $\psi_f/\psi_{fo} \in [0,2]$. As a state/disturbance estimator based on the ESM, the proposed method and its tuning procedure can also be transplanted to many industrial applications such as any areas where the disturbance meets the basic requirement shown in Section III-A and its estimation/compensation is required.

VI. CONCLUSION

This paper has presented a robust and computational efficient deadbeat PCC scheme, which estimates the nonlinear and time-varying lumped disturbance in the PMLSM electrical subsystem effectively and improves the robustness of the PCC largely.

The proposed estimator is motivated by the classical KF and the main idea of the ESO. Modeling the disturbance dynamics as an integrator subsystem removes the basic assumption and limitation that the disturbance is slowly varying as many observers designed in the literatures. Compared with the existing EKF-based TDE, the computation complexity of the ESM-based KF is reduced and then the disturbance is effectively estimated. In addition to the algorithm design, the parameter tuning method of the KF under the PCC scheme is given with the discrete simulation while only the resistance mismatch exists. Furthermore, the experimental results based on an air-bearing iron-core PMLSM test platform show the effectiveness of the ESM-KF-based PCC in the single current closed loop and the double cascade position-current control loop, of which the complex nonlinear disturbance is simulated with the controller design under the linear-varying parameter and the sine-wave current command. It is noteworthy that the proposed ESM-KF can also be transplanted to many industrial applications where the state and disturbance estimations are required.

REFERENCES

[1] D. A. Bristow and A. G. Alleyne, "A high precision motion control system with application to microscale robotic deposition," *IEEE Trans. Control Syst. Technol.*, vol. 14, no. 6, pp. 1008–1020. Nov. 2006.

[2] F. Z. Song, Y. Liu, J.-X. Xu, X. F. Yang, P. He, and Z. L. Yang, "Iterative learning identification and compensation of space-periodic disturbance in PMLSM systems with time delay," *IEEE Trans. Ind. Electron.*, vol. 65, no. 9, pp. 7579–7589, May 2018.

[3] K. Cho, J. Kim, and S. B. Choi, "A high-precision motion control based on a periodic adaptive disturbance observer in a PMLSM," *IEEE/ASME Trans. Mechatronics*, vol. 20, no. 5, pp. 2158–2171, Oct. 2015.

[4] M. Y. Wang, L. Y. Li, D. H. Pan, Y. B. Tang, and Q. B. Guo, "High-bandwidth and strong robust current regulation for PMLSM drives considering thrust ripple," *IEEE Trans. Power Electron.*, vol. 31, no. 9, pp. 6646–6657, Sep. 2016.

[5] N. Hoffmann, F. W. Fuchs, M. P. Kazmierkowski, and D. Schroder, "Digital current control in a rotating reference frame—Part I: System modeling and the discrete time-domain current controller with improved decoupling capabilities," *IEEE Trans. Power Electron.*, vol. 31, no. 7, pp. 5290–5305, Jul. 2016.

[6] S. Zhou, J. Liu, L. Zhou, and Y. Zhang, "DQ current control of voltage source converters with a decoupling method based on preprocessed reference current feed-forward," *IEEE Trans. Power Electron.*, vol. 32, no. 11, pp. 8904–8921, Nov. 2017.

[7] S. Vazquez, J. Rodriguez, M. Rivera, L. G. Franquelo, and M. Norambuena, "Model predictive control for power converters and drives: Advances and trends," *IEEE Trans. Ind. Electron.*, vol. 64, no. 2, pp. 935–947, Feb. 2017.

[8] Y. Zhang, J. Liu, H. Yang, and S. Fan, "New insights into model predictive control for three-phase power converters," *IEEE Trans. Ind. Appl.*, vol. 55, no. 2, pp. 1973–1982, Mar./Apr. 2019.

[9] H.-T. Moon H.-S. Kim, and M.-J. Youn, "A discrete-time predictive current control for PMSM," *IEEE Trans. Power Electron.*, vol. 18, no. 1, pp. 464–472, Jan. 2003.

[10] K.-H. Kim and M.-J. Youn, "A simple and robust digital current control technique of a PM synchronous motor using time delay control approach," *IEEE Trans. Power Electron.*, vol. 16, no. 1, pp. 72–82, Jan. 2001.

[11] H. Le-Huy, K. Slimani, and P. Viarouge, "Analysis and implementation of a real-time predictive current controller for permanent-magnet synchronous servo drives," *IEEE Trans. Ind. Electron.*, vol. 41, no. 1, pp. 110–117, Feb. 1994.

[12] T. Turker, U. Buyukkeles, and A. Bakan, "A robust predictive current controller for PMSM drives," *IEEE Trans. Ind. Electron.*, vol. 63, no. 6, pp. 3906–3914, Jun. 2016.

[13] K.-H. Kim, I.-C. Baik, G.-W. Moon, and M.-J. Youn, "A current control for a permanent magnet synchronous motor with a simple disturbance estimation scheme," *IEEE Control Syst. Technol.*, vol. 7, no. 5, pp. 630–633, Sep. 1999.

[14] Y. A.-R. I. Mohamed, "Design and implementation of a robust current-control scheme for a PMSM vector drive with s simple adaptive disturbance observer," *IEEE Trans. Ind. Electron.*, vol. 54, no. 4, pp. 1981–1988, Aug. 2007.

[15] X. G. Zhang, B. Hou, and Y. Mei, "Deadbeat predictive current control of permanent-magnet synchronous motors with stator current and disturbance observer," *IEEE Trans. Power Electron.*, vol. 32, no. 5, pp. 3818–3834, May 2017.

[16] B. Wang, Y. Yu, G. Wang, and D. Xu, "Static-errorless deadbeat predictive current control using second-order sliding-mode disturbance observer for induction machine drives," *IEEE Trans. Power Electron.*, vol. 33, no. 3, pp. 2395–2403, Apr. 2018.

[17] Y. J. Jiang, W. Xu, C. X. Mu, and Y. Liu, "Improved deadbeat predictive current control combined sliding mode strategy for PMSM drive system," *IEEE Trans. Veh. Technol.*, vol. 67, no. 1, pp. 251–263, Jan. 2018.

[18] J. X. Wang, F. X. Wang, G. L. Wang, S. H. Li, and L. Yu, "Generalized proportional integral observer based robust finite control set predictive current control for induction motor systems with time-varying disturbances," *IEEE Trans. Ind. Inform.*, vol. 14, no. 9, pp. 4159–4168, Sep. 2018.

[19] M. Grewal and A. Andrews, *Kalman Filtering: Theory and Practice Using MATLAB*. Hoboken, NJ, USA: Wiley–IEEE Press, 2008.

[20] R. Faragher, "Understanding the basis of the Kalman filter via a simple and intuitive derivation," *IEEE Signal Process. Mag.*, vol. 29, no. 5, pp. 128–132, Sep. 2012.

[21] F. Auger, M. Hilairet, J. M. Guerrero, E. Monmasson, T. Orlowska-Kowalska, and S. Katsura, "Industrial applications of the Kalman filter: A review," *IEEE Trans. Ind. Electron.*, vol. 60, no. 12, pp. 5458–5471, Dec. 2013.

[22] R. Dhaouadi, N. Mohan, and L. Norum, "Design and implementation of an extended Kalman filter for the state estimation of a permanent magnet synchronous motor," *IEEE Trans. Power Electron.*, vol. 6, no. 3, pp. 491–497, Sep./Oct. 1991.

[23] S. Bolognani, L. Tubiana, and M. Zigliotto, "Extended Kalman filter tuning in sensorless PMSM drives," *IEEE Trans. Ind. Appl.*, vol. 39, no. 6, pp. 1741–1747, Nov. 2003.

[24] C. Mitsantisuk, K. Ohishi, and S. Katsura, "Estimation of action/reaction forces for the bilateral control using Kalman filter," *IEEE Trans. Ind. Electron.*, vol. 59, no. 11, pp. 4383–4393, Nov. 2012.

[25] M. Ahmeid, M. Armstrong, M. Al-Greer, and S. Gadoue, "Computationally efficient self-tuning controller for DC–DC switch mode power converters based on partial update Kalman filter," *IEEE Trans. Power Electron.*, vol. 33, no. 9, pp. 8081–8090, Sep. 2018.

[26] J. R. Macias and A. G. Exposito, "Self-tuning of Kalman filters for harmonic computation," *IEEE Trans. Power Del.*, vol. 21, no. 1, pp. 501–503, Jan. 2006.

[27] M. Ahmeid, M. Armstrong, S. Gadoue, M. Algreer, and P. Missailidis, "Real time parameter estimation of DC–DC converters using a self-tuned Kalman filter," *IEEE Trans. Power Electron.*, vol. 32, no. 7, pp. 5666–5674, Jul. 2017.

[28] K. Szabat and T. Orlowska-Kowalska, "Performance improvement of industrial drives with mechanical elasticity using nonlinear adaptive Kalman filter," *IEEE Trans. Ind. Electron.*, vol. 55, no. 3, pp. 1075–1084, Mar. 2008.

[29] K. Szabat and T. Orlowska-Kowalska, "Application of the Kalman filters to the high-performance drive system with elastic coupling," *IEEE Trans. Ind. Electron.*, vol. 59, no. 11, pp. 4226–4235, Nov. 2012.

[30] D.-H. Yim, B.-G. Park, R.-Y. Kim, and D.-S. Hyun, "A predictive current control associated to EKF for high performance IPMSM drives," in *Proc. 26th Annu. IEEE Appl. Power Electron. Conf. Expo.*, 2011, pp. 1010–1016.

[31] M. Abdelrahem, C. M. Hackl, Z. B. Zhang, and R. Kennel, "Robust predictive control for direct-driven surface-mounted permanent-magnet synchronous generators without mechanical sensors," *IEEE Trans. Energy Convers.*, vol. 33, no. 1, pp. 179–189, Mar. 2018.

[32] J. Han, "From PID to active disturbance rejection control," *IEEE Trans. Ind. Electron.*, vol. 56, no. 3, pp. 900–906, Mar. 2009.

[33] H. Sira-Ramirez, A. Luviano-Juarez, M. Ramirez-Neria, and E. W. Zurita-Bustamante, *Active Disturbance Rejection Control of Dynamic Systems: A Flatness-Based Approach*. London, U.K.: Butterworth–Heinemann, 2017.

[34] M. D. Soricellis, D. D. Ru, and S. Bolognani, "A robust current control based on proportional-integral observers for permanent magnet synchronous machines," *IEEE Trans. Ind. Appl.*, vol. 54, no. 2, pp. 1437–1447, Mar. 2018.

Rui Yang was born in Hubei Province, China. He received the B.E. degree in electrical engineering, in 2015, from the Harbin Institute of Technology, Harbin, China, where he is currently working toward the Ph.D. degree in electrical engineering.

His research interests include linear motor drive and control, predictive current control, adaptive control, and sliding mode control.

Mingyi Wang was born in Jilin Province, China. He received the B.E., M.E., and Ph.D. degrees in electrical engineering from the Harbin Institute of Technology (HIT), Harbin, China, in 2009, 2011, and 2016, respectively.

He is currently with the Institute of Electromagnetic and Electronic Technology, HIT. His research interests include motor drive control, power electronic applications, and magnetic levitation.

Liyi Li (SM'17) received the B.E., M.E., and D.E. degrees from the Harbin Institute of Technology (HIT), Harbin, China, in 1991, 1995, and 2001, respectively.

Since 2004, he has been a Professor with the School of Electrical Engineering and Automation, HIT. In 2013, he became "Yangtze Fund Scholar" Distinguished Professor and is currently supported by the National Science Fund for Distinguished Young Scholars. He has authored or coauthored more than 110 technical papers and is the holder of 50 patents. His research interests include design, drive, and control of linear motors, and design and drive of high-speed/power density permanent magnet machines.

Gaolin Wang (M'13–SM'18) received the B.S., M.S., and Ph.D. degrees in electrical engineering from the Harbin Institute of Technology, Harbin, China, in 2002, 2004, and 2008, respectively.

In 2009, he joined, as a Lecturer, the Department of Electrical Engineering, Harbin Institute of Technology, where he has been a Professor of Electrical Engineering since 2014. From 2009 to 2012, he was a Postdoctoral Fellow with Shanghai STEP Electric Corporation. He has authored more than 50 technical papers published in journals and conference proceedings. He is the holder of ten Chinese patents. His research interests include permanent magnet synchronous motor drives, high-performance direct drive for traction system, position sensorless control of ac motors, and efficiency optimization control of interior PMSM.

Chengbao Zhong received the B.E. degree in mechanical engineering from the Harbin Institute of Technology, Harbin, China, in 2008.

Since 2017, he has been the Assistant Dean of the Equipment Dynamics Institute, GREE Electric Appliances Inc., Zhuhai, China. He is now a young outstanding talent of Zhuhai. He is the holder of 33 patents. His research interests include intelligent equipment core components of industrial robots and CNC machines.

Mr. Zhong was the recipient of the Gold Medal of Nuremberg International Invention Exhibition in 2018.